photonics

MDPI

Communication

# Poincaré Beams at the Tight Focus: Inseparability, Radial Spin Hall Effect, and Reverse Energy Flow

**Victor V. Kotlyar [1,2], Sergey S. Stafeev [1,2,*], Vladislav D. Zaitsev [1,2] and Alexey M. Telegin [2]**

[1] Image Processing Systems Institute of the RAS—Branch of FSRC "Crystallography & Photonics" of the RAS, 151 Molodogvardeyskaya St., 443001 Samara, Russia
[2] Samara National Research University, 34 Moskovskoe Shosse, 443086 Samara, Russia
* Correspondence: sergey.stafeev@gmail.com

**Abstract:** The family of Poincaré beams has three parameters, including two real-valued angular parameters, which specify a definite polarization state on the Poincaré sphere, and a third integer parameter $n$ specifying the beam singularity order. We show theoretically and through a numerical simulation that, while being inseparable and not allowing for the separation of polarization and orbital degrees of freedom in the general case, the Poincaré beams display remarkable properties when tightly focused. We find that at $n = 2$, a reverse energy flow occurs near the optical axis, which is mathematically expressed as the negative projection of the Poynting vector. We also reveal that given certain parameters of the Poincaré beams, the energy flow rotates around the optical axis due to spin–orbital conversion. We also reveal a radial optical Hall effect that occurs at the tight focus of Poincaré beams, when the on-axis components of the spin angular momentum vector have different signs on certain different-radius circles centered at the focal spot center.

**Keywords:** Poincaré beams; sharp focus; inseparability; radial spin Hall effect; spin angular momentum; orbital angular momentum; reverse energy flow

check for updates

**Citation:** Kotlyar, V.V.; Stafeev, S.S.; Zaitsev, V.D.; Telegin, A.M. Poincaré Beams at the Tight Focus: Inseparability, Radial Spin Hall Effect, and Reverse Energy Flow. *Photonics* **2022**, *9*, 969. https://doi.org/10.3390/photonics9120969

Received: 18 November 2022
Accepted: 8 December 2022
Published: 11 December 2022

**Publisher's Note:** MDPI stays neutral with regard to jurisdictional claims in published maps and institutional affiliations.

**Copyright:** © 2022 by the authors. Licensee MDPI, Basel, Switzerland. This article is an open access article distributed under the terms and conditions of the Creative Commons Attribution (CC BY) license (https://creativecommons.org/licenses/by/4.0/).

## 1. Introduction

Among the recipients of the 2022 Nobel Prize in physics, A. Zeilinger was recognized for research in quantum entanglement between photons. By way of illustration, his work [1] has amassed 6000+ citations. As far as photons are concerned, (hybrid) quantum entanglement (in terms of both polarization and angular momentum) implies that two photons are in superposition, and can be described by the expression [2]:

$$|\psi\rangle = a|H\rangle|l\rangle + e^{i\delta}\sqrt{1-a^2}|V\rangle|-l\rangle,$$

where $H$ and $V$ stand for the horizontal and vertical polarization vectors, $l$ is the orbital angular momentum (OAM) of photon or topological charge, $a$ is the weight coefficient (probability density of detecting the photon state), and $\delta$ is the phase delay. At $a = 1/\sqrt{2}$, the state $|\psi\rangle$ becomes fully entangled. It turns out that similar entanglement may be found in classical physics and refers to a light field described by the on-axis superposition of two vortex laser beams with different polarization states and different topological charges. Physically, a classical entangled state is when the light field is impossible to describe as a direct product $|P\rangle|OAM\rangle$, with no way to simultaneously determine a particular polarization state $|P\rangle$ and a particular OAM state $|OAM\rangle$ of the light field of interest. Hence, the light field described by the aforementioned superposition is ill-defined. In this work, we discuss an example of ill-defined light fields in the form of a wide class Poincaré beams [3,4], which include linearly and circularly polarized vortex laser beams and cylindrical vector beams [5]. Below, we show that given specific parameters, remarkable optical effects occur at the tight focus of such beams, including a reverse on-axis energy flow [6,7] and an optical Hall effect [8]. The optical Hall effect is divided into spin (SHE) [9–13], orbital [14],

and spin–orbital [15] Hall effects. An optical Hall effect occurs due to the conservation of angular momentum of light and spin–orbit interaction. As a rule, the optical Hall effect occurs because of the light–medium interaction, for instance when light reflects at a metasurface [16]. What we are more interested in is studying the SHE that occurs without the involvement of medium and microparticles, but by tightly focusing laser beams propagating in free space (see review [17]). For instance, an off-axis focal spot has been shown to be generated by passing a tightly focused vortex laser beam through an aperture [18]. In this work, analyzing the free-space propagation of Poincaré beams, we show that given specific parameters, there is a transverse energy flow at the tight focus, rotating about the optical axis clockwise or anticlockwise. We also reveal that at the tight focus, a radial spin Hall effect occurs, when on-axis spin angular momentum (SAM) projections (that may be looked considered as 'spin') have different signs on different-radius circles centered at the optical axis. That is, on the different-radius circles, vectors of elliptic polarization rotate oppositely.

## 2. Inseparability of Vector and Spatial Degrees of Freedom

In a previous work [19], we derived expressions to describe an intensity pattern from Poincaré beams at the tight focus. In this work, our purpose is to derive expressions for Poynting vector projections and an on-axis projection of the SAM at the tight focus of the Poincaré beam. However, beforehand it makes sense to discuss the topic of inseparability (entanglement) of polarization and spatial degrees of freedom of the Poincaré beam.

The light beams for which the polarization state is described by unit vectors on a Poincaré sphere are described by a Jones vector given by [3,4]:

$$\mathbf{E}_P(\varphi) = \frac{1}{\sqrt{2}}\begin{pmatrix} ae^{-in\varphi} + be^{in\varphi} \\ iae^{-in\varphi} - ibe^{in\varphi} \end{pmatrix} \tag{1}$$

where $a = \cos(\theta/2)e^{-i\psi/2}$, $b = \sin(\theta/2)e^{i\psi/2}$, $a^2 + b^2 = 1$, $\theta$ and $\psi$ are the polar and azimuthal angles on the sphere, and $n$ is an integer number that describes the topological charge of the optical vortex or the order of cylindrical (azimuthal or radial) polarization. Beam (1) can be represented as the superposition of two beams where one has right-handed and the other has left-handed polarization:

$$\frac{1}{\sqrt{2}}\begin{pmatrix} ae^{-in\varphi} + be^{in\varphi} \\ iae^{-in\varphi} - ibe^{in\varphi} \end{pmatrix} = \frac{ae^{-in\varphi}}{\sqrt{2}}\begin{pmatrix} 1 \\ i \end{pmatrix} + \frac{be^{in\varphi}}{\sqrt{2}}\begin{pmatrix} 1 \\ -i \end{pmatrix} = ae^{-in\varphi}|R\rangle + be^{in\varphi}|L\rangle, \tag{2}$$

where $|R\rangle$ and $|L\rangle$, respectively, denote Jones vectors for the right- and left-handed polarization. Considering that $a^2 + b^2 = 1$, Equation (2) can be rearranged as:

$$\mathbf{E}_p(\varphi) = \sqrt{\gamma}e^{-in\varphi}|R\rangle + \sqrt{1-\gamma}e^{in\varphi}|L\rangle, \quad \gamma = a^2. \tag{3}$$

The two quantities are said to be inseparable [20–22] when it not possible to represent the vector field as the direct product of the spatial scalar function by a Jones vector that describes the polarization state of the field. In other words, the vector field of inseparable quantities is not able to be represented as $U(r,\varphi,z)|P\rangle$, where $U(r,\varphi,z)$ is a scalar function that describes the solution of a paraxial Helmholtz equation and $|P\rangle$ is the state of transverse polarization of a paraxial light beam.

The entanglement notion is a classical analog of quantum entanglement [1,2,20–22]. The degree of inseparability is defined based on Neumann's entropy *Ent*, which, in a simple case of Equation (3), is given by:

$$Ent(E_p) = -[\gamma\log_2(\gamma) + (1-\gamma)\log_2(1-\gamma)] \tag{4}$$

Entropy in Equation (4) lies in the range $0 < Ent(E_p) < 1$. If entropy is zero, the vector field is fully separable; if entropy equals unity, the vector field is fully (maximally) insepa-

rable. At $\gamma = 1/2$, the Poincaré beam is maximally inseparable. In this case, $a = b = 1/\sqrt{2}$, which means that the Poincaré beam with maximal inseparability is identical to an $n$-th-order cylindrical vector beam:

$$\mathbf{E}_P(\varphi; a = b = 1/\sqrt{2}) = \begin{pmatrix} \cos(n\varphi) \\ \sin(n\varphi) \end{pmatrix}. \tag{5}$$

At other values of $a$ and $b$, the Poincaré beams in Equation (1) are partially inseparable, and if one of the parameters equals zero (either $a = 0$ or $b = 0$), the Poincaré beams become separable circularly polarized vortex beams. Hereinafter, we analyze what happens with beam (1) at the tight focus.

We note that exact solutions of a Helmholtz equation in spherical coordinates, as well as all six projections of the electric and magnetic fields for non-paraxial laser modes, were deduced in Ref. [23]. A linear combination of such beams produces hybrid vector beams that may be looked upon as an example of beams with partial inseparability.

## 3. Flow Energy at the Tight Focus of the Poincaré Beam

Using Richards–Wolf formalism [24], projections of the electric and magnetic fields at the tight focus of the Poincaré beam (1) can be derived in the form:

$$\begin{aligned}
E_x &= \tfrac{i^{n-1}}{\sqrt{2}}\left[\left(be^{in\varphi} + ae^{-in\varphi}\right)I_{0,n} + \left(be^{i(n-2)\varphi} + ae^{-i(n-2)\varphi}\right)I_{2,n-2}\right],\\
E_y &= \tfrac{i^{n}}{\sqrt{2}}\left[\left(ae^{-in\varphi} - be^{in\varphi}\right)I_{0,n} - \left(ae^{-i(n-2)\varphi} - be^{i(n-2)\varphi}\right)I_{2,n-2}\right],\\
E_z &= \sqrt{2}i^{n}\left(be^{i(n-1)\varphi} + ae^{-i(n-1)\varphi}\right)I_{1,n-1},\\
H_x &= \tfrac{i^{n}}{\sqrt{2}}\left[\left(be^{in\varphi} - ae^{-in\varphi}\right)I_{0,n} + \left(be^{i(n-2)\varphi} - ae^{-i(n-2)\varphi}\right)I_{2,n-2}\right],\\
H_y &= \tfrac{i^{n-1}}{\sqrt{2}}\left[\left(be^{in\varphi} + ae^{-in\varphi}\right)I_{0,n} - \left(be^{i(n-2)\varphi} + ae^{-i(n-2)\varphi}\right)I_{2,n-2}\right],\\
H_z &= \sqrt{2}i^{n+1}\left(be^{i(n-1)\varphi} - ae^{-i(n-1)\varphi}\right)I_{1,n-1}.
\end{aligned} \tag{6}$$

In Equation (6), the notation $I_{\nu,\mu}$ stands for integrals that depend just on the radial variable $r$:

$$I_{\nu,\mu} = \left(\frac{4\pi f}{\lambda}\right)\int_0^{\theta_0} \sin^{\nu+1}\left(\frac{\theta}{2}\right)\cos^{3-\nu}\left(\frac{\theta}{2}\right)\cos^{1/2}(\theta)A(\theta)e^{ikz\cos\theta}J_\mu(x)d\theta, \tag{7}$$

where $f$ is the focal length of an aplanatic optical system (an ideal spherical lens), $\lambda$ is the wavelength, $NA = \sin\theta_0$ is the numerical aperture, $J_\mu(x)$ is the Bessel function of the first kind and $\mu$th order, $x = kr\sin\theta$, and $(r, \varphi, z)$ are the cylindrical coordinates. The function $A(\theta)$ can be in the form of Gaussian or Bessel–Gaussian function or a constant (plane wave).

Using Equation (6), we can write a relationship for the intensity distribution across the focal spot:

$$\begin{aligned}
I(r,\varphi) &= |E_x|^2 + |E_y|^2 + |E_z|^2\\
&= I_{0,n}^2 + I_{2,n-2}^2 + 2I_{1,n-1}^2 + 2\sin\theta\cos(2(n-1)\varphi + \psi)\left(I_{0,n}I_{2,n-2} + 2I_{1,n-1}^2\right).
\end{aligned} \tag{8}$$

From Equation (8), it is seen that at $\sin\theta = 0$, the intensity pattern at the focus is radially symmetric and independent of the polar angle $\varphi$. Specifically, at $n = 0, 1, 2$, the focal spot forms a circle, but at $n > 2$ or $n < 0$, the focal spot forms a ring. At $\sin\theta \neq 0$, the focal spot is devoid of radial symmetry, depending on the polar angle $\varphi$ and index $n$ in Equation (8).

By using relationships for the field projections in Equation (6), we obtain Poynting vector projections (energy flow density) in the form [24]:

$$\mathbf{P} = \frac{c}{2\pi}\mathrm{Re}(\mathbf{E} * \times \mathbf{H}) \tag{9}$$

where **E** and **H** are the electric and magnetic field vectors, * denotes complex conjugation, $\times$ indicates the vector product, and $c$ is the speed of light in vacuum. Hereinafter, the constant $c/(2\pi)$ is neglected. Substituting the relationships for electromagnetic field projections at the focus in Equation (6) into Equation (9) yields:

$$\begin{aligned} P_x &= 2\left(|a|^2 - |b|^2\right)\sin(\varphi) I_{1,n-1}(I_{0,n} + I_{2,n-2}), \\ P_y &= -2\left(|a|^2 - |b|^2\right)\cos(\varphi) I_{1,n-1}(I_{0,n} + I_{2,n-2}), \\ P_z &= I_{0,n}^2 - I_{2,n-2}^2. \end{aligned} \tag{10}$$

In view of the relationships for the parameters $a$ and $b$ from Equation (1), the Poynting vector projections of Equation (10) at the focus can be rewritten as:

$$\begin{aligned} P_x &= 2\cos(\theta)\sin(\varphi) I_{1,n-1}(I_{0,n} + I_{2,n-2}), \\ P_y &= -2\cos(\theta)\cos(\varphi) I_{1,n-1}(I_{0,n} + I_{2,n-2}), \\ P_z &= I_{0,n}^2 - I_{2,n-2}^2. \end{aligned} \tag{11}$$

In Equation (11), the angle $\theta$ is a parameter that defines a point on the Poincaré sphere of polarization states. The transverse Poynting vector projections in Equation (11) can be converted from the Cartesian to the polar coordinates, with Equation (11) transformed into:

$$\begin{aligned} P_r &= 0, \\ P_\varphi &= -\cos(\theta) I_{1,n-1}(I_{0,n} + I_{2,n-2}), \\ P_z &= I_{0,n}^2 - I_{2,n-2}^2. \end{aligned} \tag{12}$$

An analysis of Equation (12) affords the following conclusions. With the on-axis Poynting vector component depending only on the radial coordinate, the distribution of the energy flow propagating along the optical axis becomes circularly symmetric for any parameters ($a$, $b$) or ($\theta$, $\psi$). Interestingly, at $n$ = 2, it follows from Equation (12) that near the optical axis in the focal plane, a reverse energy flow occurs:

$$\begin{aligned} P_{z,2}(r) &= -I_{2,0}^2 + I_{0,2}^2, \\ P_{z,2}(r=0) &= -I_{2,0}^2 < 0. \end{aligned} \tag{13}$$

The second equality in Equation (13) stems from the fact that among the integrals entering Equation (7), only those with zero second index ($\mu$ = 0) remain non-zero on the optical axis ($r$ = 0). This is because only the zero-order Bessel function is non-zero at the origin: $J_0(0)$ = 1. Equation (13) suggests that an on-axis reverse flow will occur when tightly focusing a multitude of initial optical fields, including a second-order optical vortex with left-handed circular polarization, $\exp(i2\varphi)(1, -i)^T$, where $T$ denotes vector transposition, a minus second-order optical vortex with right-handed circular polarization $\exp(-i2\,\varphi)(1,i)^T$, a second-order radially polarized vector field $(\cos(2\,\varphi), \sin(2\,\varphi))^T$, a second-order azimuthally polarized optical field, $(-\sin(2\,\varphi), \cos(2\,\varphi))^T$, and so on. Previously, the reverse energy flow at the tight focus was discussed in Refs. [6,7].

From Equation (12), it also follows that at $\cos\theta \neq 0$, the near-axis transverse energy flow at the focus is rotating clockwise at $\cos\theta > 0$ and anticlockwise at $\cos\theta < 0$.

At $\cos\theta = 0$, the energy flow at the focal plane is laminar (the transverse Poynting vector component is zero) and not rotating. Given that $\cos\theta \neq 0$ (meaning that elliptic polarization is found in the source field), the transverse energy flow at the tight focus of Poincaré beams will rotate around the optical axis at any topological charge $n$ due to spin–orbital conversion. At $\cos\theta > 0$ and $n = 0$, the energy flow will rotate anticlockwise and clockwise at $n > 0$.

## 4. Spin Angular Momentum at the Tight Focus of Poincaré Beams

In this section, we derive the spin angular momentum (SAM) of the Poincaré beam (1) at the focus. The spin density vector is calculated using a familiar formula [25]:

$$\mathbf{S} = \frac{1}{8\pi\omega}\mathrm{Im}(\mathbf{E}* \times \mathbf{E}) \tag{14}$$

where $\omega$ is the cyclic frequency of light. Hereinafter, the constant $1/(8\pi\omega)$ is neglected. From (14), the on-axis SAM component (without regard for the constant) is seen to coincide with the third Stokes vector component, $s_3$:

$$s_3 = S_z = 2\mathrm{Im}\left(E_x^* E_y\right) \tag{15}$$

Thus, we infer that it is the on-axis SAM component that indicates the field at the focus is circularly or elliptically polarized. Substituting the electric field projections (6) into (15) yields:

$$S_z = \left(|a|^2 - |b|^2\right)\left[I_{0,n}^2 - I_{2,n-2}^2\right] \tag{16}$$

For the source Poincaré field (1), the on-axis SAM component is given by:

$$S_{z,in} = |a|^2 - |b|^2 = \cos\theta. \tag{17}$$

From Equations (16) and (17), the initial homogeneous spin density, defined by $\cos\theta$, is seen at the focus to become inhomogeneous, as well as changing sign and taking a zero value at certain radii. The radius-dependent separation of regions with the opposite sign of spin (16) may be interpreted as a radial spin Hall effect for all $n$. If, in the initial plane, the spin density is zero ($\cos\theta = 0$), then at the focus the on-axis spin density component of Equation (16) will also be zero. If the original spin in (17) is positive ($\cos\theta > 0$), i.e., the initial polarization vector rotates anticlockwise (Equation (12), then, given $n = 0$, the transverse energy flow at the focus will also rotate anticlockwise thanks to the spin–orbital conversion.

## 5. Orbital Angular Momentum at the Tight Focus of Poincaré Beams

Now, let us analyze the behavior of the angular momentum at the tight focus of a Poincaré beam (1). The angular momentum is given by [26]:

$$\mathbf{J} = \frac{1}{2c}\mathrm{Re}(\mathbf{r} \times (\mathbf{E}^* \times \mathbf{H})) = \frac{2\pi}{c^2}(\mathbf{r} \times \mathbf{P}) \tag{18}$$

where $\mathbf{r}$ is the radius vector and $c$ is the speed of light in vacuum. Dropping the constant $2\pi/c^2$ in Equation (18) and considering Equation (12), the on-axis projection of the angular momentum vector (18) takes the form:

$$J_z = rP_\varphi = -r\cos(\theta)I_{1,n-1}(I_{0,n} + I_{2,n-2}). \tag{19}$$

From Equation (19), the angular momentum is seen to always be zero on the optical axis at $r = 0$, because the "arm" is zero. The angular momentum is the sum of the SAM and the orbital angular momentum (OAM) [26]:

$$\mathbf{J} = \mathbf{S} + \mathbf{L} = \frac{1}{8\pi\omega}\mathrm{Im}(\mathbf{E}^* \times \mathbf{E}) + \frac{1}{8\pi\omega}\sum_{p=x,y,z}\mathrm{Im}\left(E_p^*(\mathbf{r} \times \nabla)E_p\right) \tag{20}$$

Dropping the constant $1/(8\pi\omega)$ from Equation (20) and taking into account Equations (16) and (19), the relation for the on-axis component $L_z$ of the OAM density takes the form:

$$L_z = -\cos(\theta)\left[rI_{1,n-1}(I_{0,n} + I_{2,n-2}) + I_{0,n}^2 - I_{2,n-2}^2\right]. \tag{21}$$

Equation (21) suggests that if the source Poincaré beam has zero spin ($\cos\theta = 0$), the OAM is zero at the focus ($L_z = 0$). If, however, the source Poincaré beam has non-zero spin ($\cos\theta \neq 0$), both the angular momentum (19) and OAM (21) occur at the focus.

## 6. Numerical Modeling

The numerical simulation in this section is based on calculating the Debye integral using a Richards–Wolf method [24]. The focusing is assumed to be conducted with an aplanatic objective with NA = 0.95 for a wavelength of $\lambda = 0.532$ nm. Figure 1 depicts intensity patterns $I = |E_x|^2 + |E_y|^2 + |E_z|^2$ at the tight focus of a Poincaré beam at the parameters $\theta = \pi/4$, $\psi = \pi/4$, $n = 0$ (non-vortex elliptically polarized beam, Figure 1a); $\theta = 0$, $\psi = \pi/2$, $n = 0$ (non-vortex right-handed circularly polarized beam, Figure 1b); $\theta = \pi/4$, $\psi = \pi/4$, $n = 1$ (elliptically polarized vortex, Figure 1c); and $\theta = 0$, $\psi = 0$, $n = -1$ (right-handed circularly polarized vortex, Figure 1d).

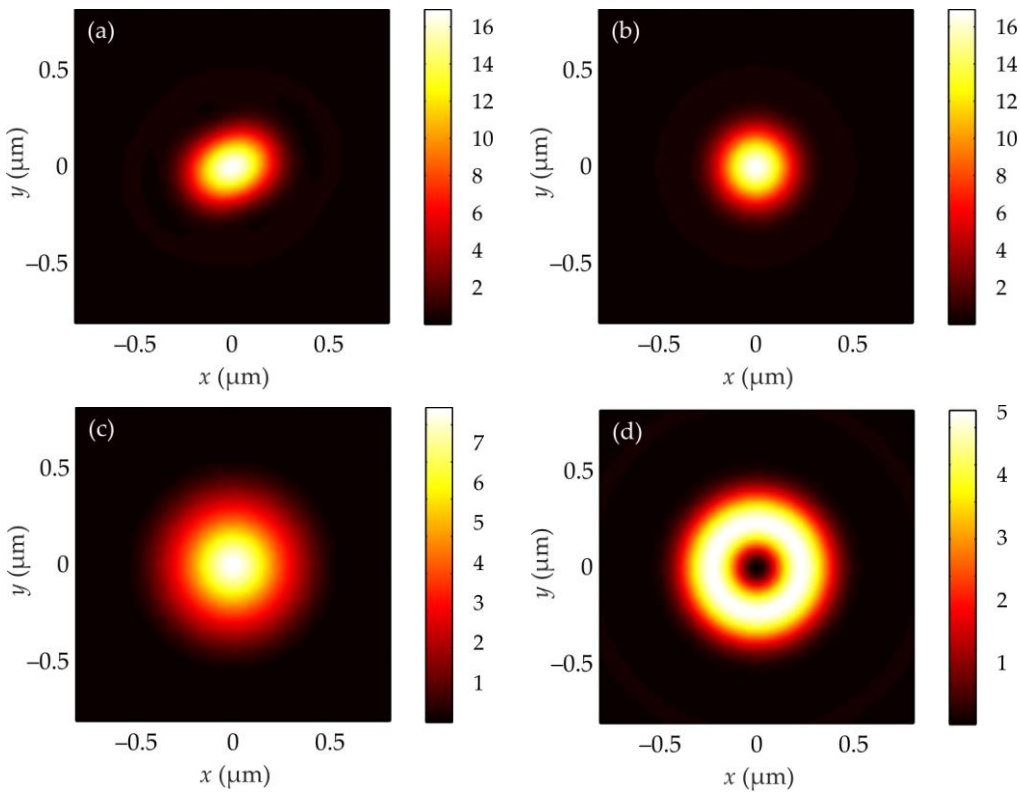


**Figure 1.** Intensity patterns at the focus for different Poincaré beams of Equation (1): $\theta = \pi/4$, $\psi = \pi/4$, $n = 0$ (**a**); $\theta = 0$, $\psi = \pi/2$, $n = 0$ (**b**); $\theta = \pi/4$, $\psi = \pi/4$, $n = 1$ (**c**); $\theta = 0$, $\psi = 0$, $n = -1$ (**d**).

From Figure 1, beams with elliptical (a), circular (b), and near-radial (c) polarization are seen to produce an elliptic or circular focal spot, whereas a vortex beam with circular polarization (d) produces an annular focal spot. Such types of intensity patterns agree well with Equation (8).

Figure 2 depicts transverse Poynting vector components $P_x$ (a,d) and $P_y$ (b,e) at the foci of two out of the four beams shown in Figure 1. The energy flow in Figure 1a for the beam with the parameters $\theta = \pi/4$, $\psi = \pi/4$, $n = 0$ is identical to those for the beams with $\theta = \pi/4$, $\psi = \pi/4$, $n = 1$ (c) and $\theta = 0$, $\psi = 0$, $n = -1$ (d). From Figure 2a,b, the transverse energy flows at the focus are seen to be rotating anticlockwise for these three beams. Meanwhile, the transverse energy flow produced by the beam with $\pi/4$, $\psi = \pi/4$, $n = 1$ (Figure 2d,e) will experience clockwise rotation. This may be concluded from Equation (12), because at $n = 0, -1$ the angular projection of the near-axis energy flow ($kr < 1$) is positive: $P_\varphi = \cos(\theta) I_{1,1}(I_{0,0} + I_{2,2}) > 0$, $P_\varphi = \cos(\theta) I_{1,2}(I_{0,1} + I_{2,3}) > 0$, becoming negative at

$n = 1$: $P_\varphi = -\cos(\theta) I_{1,0}(I_{0,1} - I_{2,1}) < 0$. The only situation when the energy flow does not rotate is at $\cos\theta = 0$.

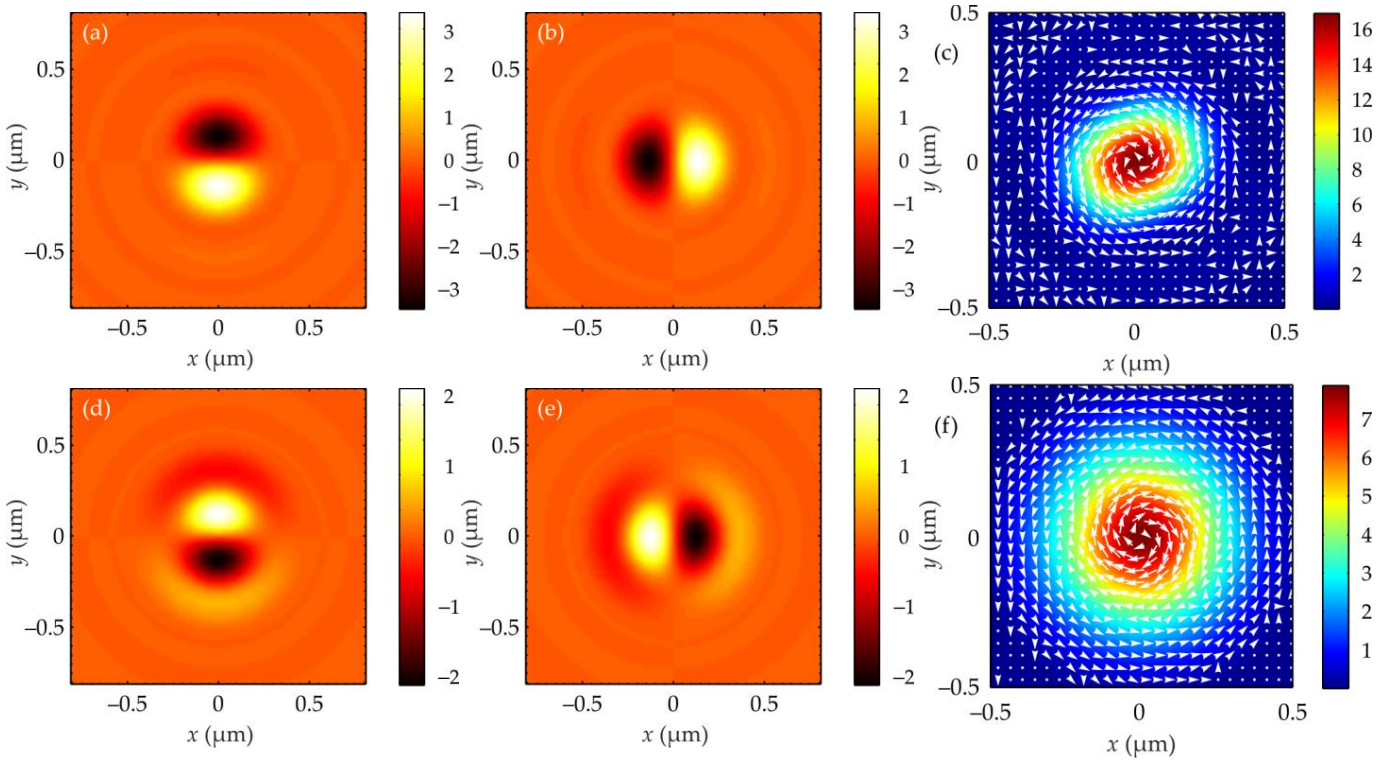


**Figure 2.** Patterns of the transverse energy flow (Poynting vector projections) at the tight focus: $P_x$ (**a**,**d**), $P_y$ (**b**,**e**) and the direction (arrows) of rotation of the transverse energy flow against the intensity background (**c**,**f**) for two different Poincaré beams: $\theta = \pi/4$, $\psi = \pi/4$, $n = 0$ (**a**,**b**,**c**); $\theta = \pi/4$, $\psi = \pi/4$, $n = 1$ (**d**,**e**,**f**).

Figure 3 depicts patterns of the on-axis SAM vector component (16) at the foci of two beams with the parameters: $\theta = \pi/4$, $\psi = \pi/4$, $n = 0$ (a,b); $\theta = \pi/4$, $\psi = \pi/4$, $n = 1$ (c,d). We note that the beam with the parameters $\theta = 0$, $\psi = \pi/2$, $n = 0$ produces a SAM pattern similar to that in Figure 3a, with the beam at $\theta = 0$, $\psi = 0$, $n = -1$ producing a pattern of the on-axis SAM projection analogous to that in Figure 3c. This conclusion follows from Equation (16), because at $n = 0$, the on-axis SAM projection does not take zero values, $S_z(r = 0) = \cos\theta\left[I_{0,0}^2 - I_{2,2}^2\right] \neq 0$; meanwhile at $n = 1$, everywhere on the optical axis the SAM projection is zero, $S_z(r = 0) = \cos\theta\left[I_{0,1}^2 - I_{2,1}^2\right] = 0$, as is the case at $n = -1$, $S_z(r = 0) = \cos\theta\left[I_{0,1}^2 - I_{2,3}^2\right] = 0$.

Figure 3b,d,f show sections along the $x$-axis of the axial projection of the SAM vector. It can be seen from Figure 3b,d that at some distance from the optical axis, the SAM projection becomes negative (see enlarged fragments). In Figure 3f, negative SAM values appear near the optical axis. Negative values of the longitudinal projection of the SAM take place in those places of the focus plane where the axial energy flow is negative, since it follows from (12) and (16) that:

$$S_z = P_z \cos\theta \tag{22}$$

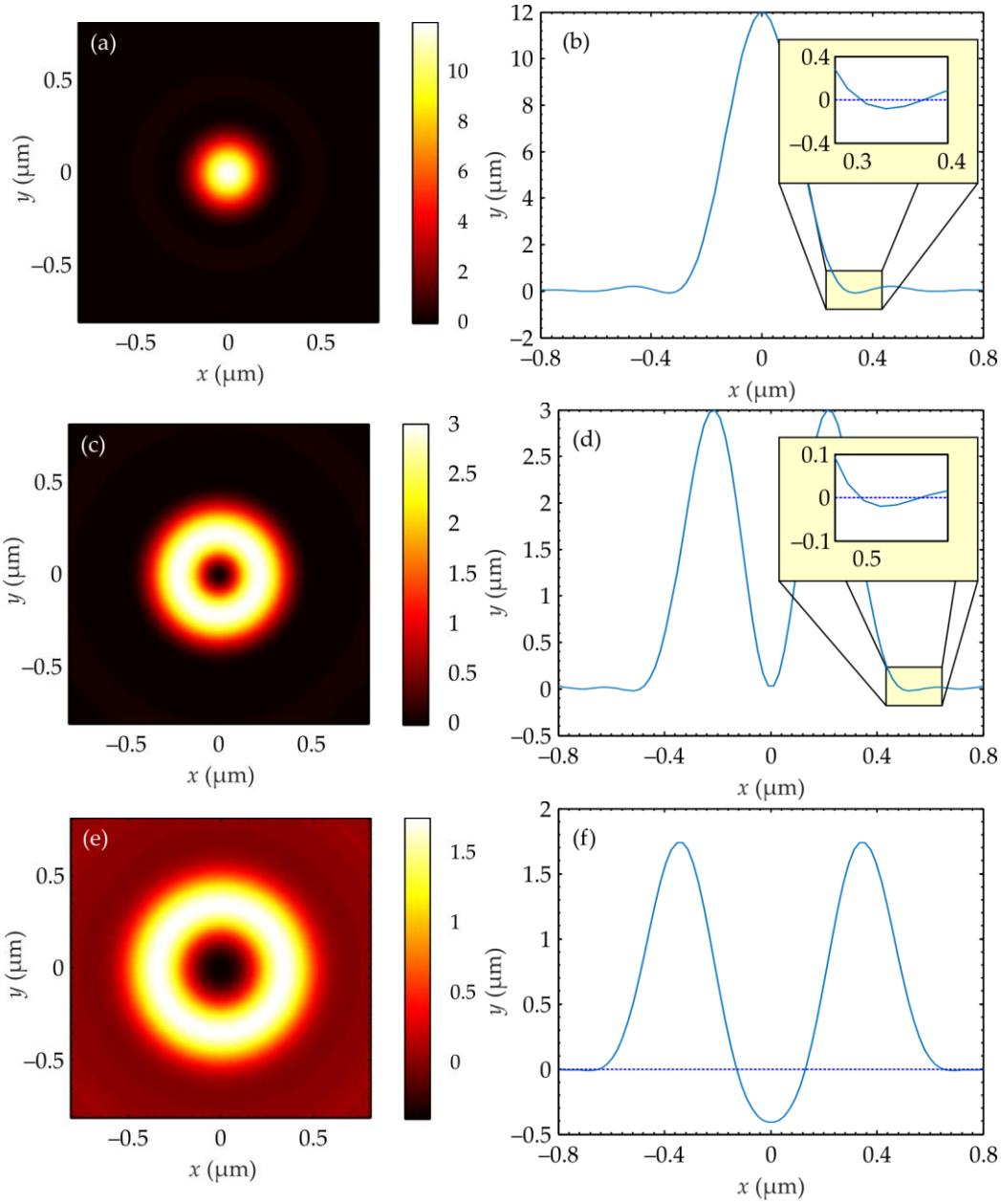


**Figure 3.** Distributions of the axial projection of the SAM ($S_z$) and their cross-sections along the $x$-axis for three different Poincaré beams: $\theta = \pi/4$, $\psi = \pi/4$, $n = 0$ (**a**,**b**); $\theta = \pi/4$, $\psi = \pi/4$, $n = 1$ (**c**,**d**); $\theta = \pi/4$, $\psi = \pi/4$, $n = 2$ (**e**,**f**).

## 7. Conclusions

In this work, we obtained the following new results. Using a relationship for von Neumann entropy it has been shown that the family of Poincare beams represents a classical entangled (nonseparable) state of light. The entanglement has been shown to become maximal when the Poincaré beams are reduced to cylindrical $n$-th-order vector beams, Equation (5). Classical entanglement, or nonseparability, of a light beam implies that polarization and orbital degrees of freedom cannot be separated. However, at certain parameters, the Poincaré beams are fully separable, in which case they are reduced to left- or right-handed circularly polarized vortex beams. The Poincaré beams show remarkable properties at the tight focus. Namely, at $n = 2$, a near-axis reverse energy flow has been found to occur when the on-axis Poynting vector component is negative, Equation (13). Given certain parameters of the Poincaré beam ($\cos\theta \neq 0$), the transverse energy flow has

been found to rotate around the optical axis at any topological charge $n$ thanks to spin–orbital conversion, Equation (12). More specifically, the energy flow rotates anticlockwise at $\cos\theta > 0$ and $n = 0$, rotating clockwise at $n > 0$. The condition $\cos\theta \neq 0$ means that in the source plane, the on-axis SAM component of Poincaré beams is non-zero, Equation (17). In this case, at the focus, a non-zero on-axis SAM component with alternating sign is also observed, Equation (16), that can take zero values on certain radii. Radius-dependent separation of focal regions with alternating sign of spin density (16) can be interpreted as a radial spin Hall effect for all $n$. Finally, it has been revealed that thanks to spin–orbital conversion, a non-zero on-axis component of the OAM vector occurs at the focus of Poincaré beams, Equation (21).

In conclusion, it is worth noting that the optical spin Hall effect, which manifests itself as the propagation of left- and right-hand elliptically polarized light fields at different angles to the optical axis (Figure 3), is closely related to the optical Magnus effect [27]. The latter occurs upon propagation of (i) circularly polarized optical beams in a multimode fiber [27] or (ii) circularly polarized optical vortices in a uniaxial crystal [28]. The optical Magnus effect consists in the propagation of left- and right-hand circularly polarized optical beams at different angles in the inhomogeneous or anisotropic medium and is caused by geometrical Berry phase anisotropy [29].

Finally, we note that Poincaré beams can be generated with the aid of spatial light modulators (SLM) [30], metasurfaces [31], and $q$-plates in a laser cavity [32].

**Author Contributions:** Conceptualization, V.V.K.; methodology, V.V.K. and S.S.S.; software, S.S.S., V.D.Z. and A.M.T.; validation, V.V.K.; formal analysis, V.V.K.; investigation, V.V.K., S.S.S., V.D.Z. and A.M.T.; resources, S.S.S.; data curation, S.S.S.; writing—original draft preparation, V.V.K.; writing—review and editing, V.V.K.; visualization, S.S.S. and V.D.Z.; supervision, V.V.K.; project administration, V.V.K.; funding acquisition, V.V.K. All authors have read and agreed to the published version of the manuscript.

**Funding:** This work was funded by the Russian Science Foundation under Project No. 22-12-00137.

**Institutional Review Board Statement:** Not applicable.

**Informed Consent Statement:** Not applicable.

**Data Availability Statement:** Not applicable.

**Conflicts of Interest:** The authors declare no conflict of interest.

## References

1. Bouwmeester, D.; Pan, J.W.; Mattle, K.; Eibl, M.; Weinfurter, H.; Zeilinger, A. Experimental quantum teleportation. *Philos. Trans. R. Soc. A Math. Phys. Eng. Sci.* **1998**, *356*, 1733–1737. [CrossRef]
2. Fickler, R.; Campbell, G.; Buchler, B.; Lam, P.K.; Zeilinger, A. Quantum entanglement of angular momentum states with quantum numbers up to 10,010. *Proc. Natl. Acad. Sci. USA* **2016**, *113*, 13642–13647. [CrossRef] [PubMed]
3. Beckley, A.M.; Brown, T.G.; Alonso, M.A. Full Poincaré beams. *Opt. Express* **2010**, *18*, 10777. [CrossRef] [PubMed]
4. Chen, S.; Zhou, X.; Liu, Y.; Ling, X.; Luo, H.; Wen, S. Generation of arbitrary cylindrical vector beams on the higher order Poincaré sphere. *Opt. Lett.* **2014**, *39*, 5274–5276. [CrossRef]
5. Zhan, Q. Cylindrical vector beams: From mathematical concepts to applications. *Adv. Opt. Photonics* **2009**, *1*, 1–57. [CrossRef]
6. Kotlyar, V.V.; Kovalev, A.A.; Nalimov, A.G. Energy density and energy flux in the focus of an optical vortex: Reverse flux of light energy. *Opt. Lett.* **2018**, *43*, 2921–2924. [CrossRef]
7. Kotlyar, V.V.; Stafeev, S.S.; Kovalev, A.A. Reverse and toroidal flux of light fields with both phase and polarization higher-order singularities in the sharp focus area. *Opt. Express* **2019**, *27*, 16689–16702. [CrossRef]
8. Leyder, C.; Romanelli, M.; Karr, J.P.; Giacobino, E.; Liew, T.C.H.; Glazov, M.M.; Kavokin, A.V.; Malpuech, G.; Bramati, A. Observation of the optical spin hall effect. *Nat. Phys.* **2007**, *3*, 628–631. [CrossRef]
9. Yin, X.; Ye, Z.; Rho, J.; Wang, Y.; Zhang, X. Photonic spin hall effect at metasurfaces. *Science* **2013**, *339*, 1405–1407. [CrossRef]
10. Nath Baitha, M.; Kim, K. All angle polarization-independent photonic spin Hall effect. *Opt. Laser Technol.* **2022**, *156*, 108458. [CrossRef]
11. Li, S.-M.; Chen, J. Spin Hall effect of reflected light from an air-glass interface around the Brewster's angle. *Appl. Phys. Lett.* **2012**, *100*, 071109. [CrossRef]

12. Roy, B.; Ghosh, N.; Banerjee, A.; Gupta, S.D.; Roy, S. Manifestations of geometric phase and enhanced spin Hall shifts in an optical trap. *New J. Phys.* **2014**, *16*, 083037. [CrossRef]
13. Kumar, R.N.; Yatish; Gupta, S.D.; Ghosh, N.; Banerjee, A. Probing the rotational spin-Hall effect in a structured Gaussian beam. *Phys. Rev. A* **2022**, *105*, 023503. [CrossRef]
14. Zhang, J.; Zhou, X.-X.; Ling, X.-H.; Chen, S.-Z.; Luo, H.-L.; Wen, S.-C. Orbit-orbit interaction and photonic orbital Hall effect in reflection of a light beam. *Chin. Phys. B* **2014**, *23*, 064215. [CrossRef]
15. He, Y.; Xie, Z.; Yang, B.; Chen, X.; Liu, J.; Ye, H.; Zhou, X.; Li, Y.; Chen, S.; Fan, D. Controllable photonic spin Hall effect with phase function construction. *Photonics Res.* **2020**, *8*, 963. [CrossRef]
16. Fu, S.; Guo, C.; Liu, G.; Li, Y.; Yin, H.; Li, Z.; Chen, Z. Spin-orbit optical hall effect. *Phys. Rev. Lett.* **2019**, *123*, 243904. [CrossRef]
17. Ling, X.; Zhou, X.; Huang, K.; Liu, Y.; Qiu, C.-W.; Luo, H.; Wen, S. Recent advances in the spin Hall effect of light. *Rep. Prog. Phys.* **2017**, *80*, 066401. [CrossRef]
18. Ling, X.; Yi, X.; Zhou, X.; Liu, Y.; Shu, W.; Luo, H.; Wen, S. Realization of tunable spin-dependent splitting in intrinsic photonic spin Hall effect. *Appl. Phys. Lett.* **2014**, *105*, 151101. [CrossRef]
19. Kotlyar, V.V.; Kovalev, A.A.; Stafeev, S.S.; Zaitsev, V.D. Index of the polarization singularity of Poincare beams. *Bull. Russ. Acad. Sci. Phys.* **2022**, *86*, 1158–1163. [CrossRef]
20. Borges, C.V.S.; Hor-Meyll, M.; Huguenin, J.A.O.; Khoury, A.Z. Bell-like inequality for the spin-orbit separability of a laser beam. *Phys. Rev. A* **2010**, *82*, 033833. [CrossRef]
21. Otte, E.; Rosales-Guzmán, C.; Ndagano, B.; Denz, C.; Forbes, A. Entanglement beating in free space through spin–orbit coupling. *Light Sci. Appl.* **2018**, *7*, 18009. [CrossRef] [PubMed]
22. McLaren, M.; Konrad, T.; Forbes, A. Measuring the nonseparability of vector vortex beams. *Phys. Rev. A* **2015**, *92*, 023833. [CrossRef]
23. Volyar, A.V.; Shvedov, V.G.; Fadeeva, T.A. Structure of a nonparaxial Gaussian beam near the focus: III stability, eigenmodes, and vortices. *Opt. Spectr.* **2001**, *91*, 235–245. [CrossRef]
24. Richards, B.; Wolf, E. Electromagnetic diffraction in optical systems. II. Structure of the image field in an aplanatic system. *Proc. R. Soc. A Math. Phys. Eng. Sci.* **1959**, *253*, 358–379. [CrossRef]
25. Bliokh, K.Y.; Ostrovskaya, E.A.; Alonso, M.A.; Rodríguez-Herrera, O.G.; Lara, D.; Dainty, C. Spin-to-orbital angular momentum conversion in focusing, scattering, and imaging systems. *Opt. Express* **2011**, *19*, 26132. [CrossRef]
26. Bliokh, K.Y.; Bekshaev, A.Y.; Nori, F. Extraordinary momentum and spin in evanescent waves. *Nat. Commun.* **2014**, *5*, 3300. [CrossRef]
27. Dooghin, A.V.; Kundikova, N.D.; Liberman, V.S.; Zel'Dovich, B.Y. Optical Magnus effect. *Phys. Rev. A* **1992**, *45*, 8204. [CrossRef]
28. Fadeyeva, T.A.; Rubass, A.F.; Volyar, A.V. Transverse shift of a high-order paraxial vortex-beam induced by a homogeneous anisotropic medium. *Phys. Rev. A* **2009**, *79*, 053815. [CrossRef]
29. Bliokh, K.Y.; Bliokh, Y.P. Optical Magnus effect as a consequence of Berry phase anisotropy. *JEPT Lett.* **2004**, *79*, 519–522. [CrossRef]
30. Gu, Z.; Yin, D.; Gu, F.; Zhang, Y.; Nie, S.; Feng, S.; Ma, J.; Yuan, C. Generation of concentric perfect Poincaré beams. *Sci. Rep.* **2019**, *9*, 15301. [CrossRef]
31. Liu, M.; Huo, P.; Zhu, W.; Zhang, C.; Zhang, S.; Song, M.; Zhang, S.; Zhou, Q.; Chen, L.; Lezec, H.J.; et al. Broadband generation of perfect Poincaré beams via dielectric spin-multiplexed metasurface. *Nat. Commun.* **2021**, *12*, 2230. [CrossRef] [PubMed]
32. Naidoo, D.; Roux, F.S.; Dudley, A.; Litvin, I.; Piccirillo, B.; Marrucci, L.; Forbes, A. Controlled generation of higher-order Poincaré sphere beams from a laser. *Nat. Photonics* **2016**, *10*, 327–332. [CrossRef]